Theoretical Interpretations of Electronic and Fluorescence Spectra of New 2(1*H*)-Pyridone Derivatives in Solution and Solid State

Yasuhiro Shigemitsu[a,b*], Masayori Hagimori[c], Naoko Mizuyama[d], Bo-Cheng Wang[e], Yoshinori Tominaga[d]

[a]*Industrial Technology Center of Nagasaki, 2-1303-8, Ikeda, Omura, Nagasaki 856-0026, Japan*

[b]*Graduate School of Engineering, Nagasaki University, 1-14, Bunkyo-machi, Nagasaki 852-8131, Japan*

[c]*Faculty of Pharmaceutical Sciences, Kobe Pharmaceutical University, 4-19-1 Motoyamakita Machi, Higashinada Ku, Kobe 658-8558, Japan*

[d]*Faculty of Environmental Studies, Nagasaki University, 1-14, Bunkyo-machi, Nagasaki 852-8131, Japan*

[e]*Department of Chemistry, Tamkang University, Tamsui 251, Taiwan*

Correspondence author: Tel:+81-957-52-1133; fax:+81-057-52-1136.

E-mail address: shige@tc.nagasaki.go.jp (Y.Shigemitsu)

A combined experimental and computational study was performed for the spectroscopic properties of novel 2(*1H*)-pyridones. The compounds were found to be virtually non-fluorescence in solution while modestly fluorescent in solid state. The solvent effects on the UV-vis and fluorescence maxima were estimated by means of a series of ab-initio quantum chemical calculations in conjunction with Polarizable Continuum Model (PCM) method. Influence of structural displacements and intermolecular interactions in crystalline state were examined in details on the spectra of two representative compounds by using Fragment Molecular Orbital (FMO) scheme. The FMO pair interaction analysis of the spectra indicate that (1) intermolecular hydrogen bonds provoke bathochromic shifts (2) electrostatic interactions induce hypsochomic shifts (3) crystal packing effects induce hypsochomic shifts in total from the maxima in vacuo.

Keywords: 2(1*H*)-pyridones; quantum chemical calculations; electronic spectra; solid-state fluorescence

1. Introduction

Spectroscopic properties of functional dyes have been widely studied and their fluorescence in solid state has attracted much attention owing to organic light-emitting diode (OLED) applications [1-5]. In general, fluorescent compounds show intense luminescence in dilute solution while fairly weak or nonluminescent in the crystalline state [6], due to enhanced non-emissive deactivation channels such as exciton/excimer formation, vibronic interactions and other nonradiative decay processes in aggregated states. Interestingly, many opposite phenomena have been reported today to the conventional emission quenching, where strong luminescence is observed in the solid state whereas negligible luminescence in dilute solution. This anomaly is called Aggregation Induced Emission Enhancement (AIEE) [7-9].

From theoretical viewpoints, a sophisticated treatment of a large condensed phase system is required to understand AIEE and such state-of-the-art methodologies are still being developed. In order to circumvent huge computational costs in direct treatment of a whole system, modern quantum chemistry techniques are based on the idea to divide them into fragments [10-11] or to hybridize several theoretical levels allocated to multiply divided layers such as QM/MM (quantum mechanics/molecular mechanics) [12] or ONIOM (Our Own N-layered Integrated Molecular Orbital) [13].

Various pyridine derivatives including 2-aminopyridine and 2,2'-bipyridyl have been extensively utilized as chelating reagents to effectively form complexes with various metals [14]. *4H*-pyrone derivatives were reported to serve as potential OLED materials [15]. In the course of our study, the structure-fluorescence relationship were elucidated for 6-aryl-*2H*-pyran-2-one derivatives bearing push-pull intramolecular charge transfer systems which showed fluorescence both in solution and in the solid phase [16]. The synthesis and fluorescent properties of novel 5-aryl-2,2'-bipyridyls were presented as well as the X-ray structural analysis and the computational studies [17].

Herein, we report and discuss the synthesis, spectroscopic properties and computational studies of new 2(*1H*)-pyridones, 1-substituted 6-aryl-2(*1H*)-pyridone and 6-aryl-2-methoxypyridine derivatives. The computational analysis is focused on the condensed phase effects exerting on the spectroscopic properties, by means of ONIOM and FMO methods to evaluate the electronic structures in

solution as well as in the crystalline phase. From physicochemical viewpoints, 2(*1H*)-pyridone, the simplest compound, has attracted much attention on its keto-enol tautomerism associated with inter- and intra-molecular hydrogen atom transfer, and been examined in detail on the rotational Duschinsky effect [18], cluster structures in solvents [19], phase transition in solid state [20]. Borst et al. reported that the complex of the two tautomers showed stronger fluorescence than solely respective species [21]. The compounds possess medical properties found in antibacterial antifungal as potential drug candidates for various diseases [22-23].

This article is organized as follows. The synthesis and spectroscopic properties are concisely described and followed by the computational details. The calculation results are presented and discussed on the UV-vis and fluorescence of the compounds both in solution and in the solid state, then brief conclusions are presented.

2. Syntheses, UV-vis and fluorescence spectra

A convenient synthesis of poly functionalized-2(*1H*)-pyridones through the reaction of various methyl ketones with ketene dithioacetals has been reported previously [24]. It has been found that ketene dithioacetals are useful and convenient reagents for the synthesis of a variety of heterocycles [25]. Figure 1 illustrates the synthetic scheme of the present study, whereby the reactions occurred smoothly in the presence of sodium hydroxide in dimethylsulfoxide to give 6-aryl-4-methylsulfanyl-2(*1H*)-pyridone-3-carbonitriles **3**, which were further converted into 6-aryl-4-pyrrolidino-2(*1H*)-pyridones **5**, 2-methoxypyridine **6** and 1-methyl-2(*1H*)-pyridone **7**. One-pot synthesis was attempted instead of the selective methylation [26] to obtain both **6** and **7**, which were separated easily upon eluting silica-gel column. 1-Methyl-4-pyrrolidono-2(*1H*)-pyridones **8** were obtained from **7** via the reactions with pyrrolidine, as illustrated in Fig.1, 2 and 3.

The measurement of absorption and fluorescence spectra was carried out at room temperature in ethanol and in the solid state, respectively. Absorption maxima, molar absorption, fluorescence maxima, and relative fluorescence intensities in the solid state are listed in Tables 1, 2 and 3. In ethanol, **3f**, some 2-methoxypyridines **6** and **7f** were found to be slightly fluorescent with their quantum yields less than 0.03. Remaining 2(*1H*)-pyridones **3** and 1-methyl-2(*1H*)-pyridones **7** were non-fluorescent. In general, sulfur atoms in fluorescent compounds generally weaken emission intensities due to spin orbit couplings [17][27]. In the solid state, the fluorescence properties of 2(*1H*)-pyridone are expected to be influenced by both the electronic and the steric effect of substituents, as shown in a previous

study of 2(*1H*)-pyrones [16]. Compound **3b** with an electron-donating group at position 4 on the phenyl ring showed enhanced emission with Relative Intensity (R.I.) of 1.28, significantly larger than that of **3a** (0.99). The fluorescent intensity of 6-(3,4-dimethoxyphenyl)-2(*1H*)-pyridone **3c** and 3,4,5-trimethoxy-2(*1H*)-pyridone **3e** remain unchanged qualitatively. 6-styryl-2(*1H*)-pyridone **3k** and 6-(4-dimethylaminophenyl)vinyl-2(*1H*)-pyridone **3l** showed their emission maxima at 560 nm and 564 nm, respectively, with a significant bathochromic shift from other **3** series, owing to an analogous chromophore with 4-(dicyanomethylene)-2-methyl-6-(p-dimethylaminostyryl)-*4H*-pyran (DCM). 2-methoxypyridines **6** and the corresponding 1-Methyl-2(*1H*)-pyridones **7**, derived from the respective 2-pyridine proton tautomers, have almost the same fluorescence characteristics, in that the introduction of a methoxy group to the phenyl ring (**7b**) enhances the fluorescence in comparison with **7a** and a significant bathochromic shift was observed via the introduction of styryl group **7k**.

The details of synthesis and spectroscopic measurements are described in Experimental section.

3. Computational details

Ground state geometry optimizations of the single molecules at DFT level were carried out using B3LYP[28][29] functional with 6-311G(2d,2p) and S_1 state geometries were optimized using TDDFT(B3LYP)/6-31+G(d), respectively, with the default convergence criterion on force and displacement. The optimized geometries were validated with vibrational frequency analysis for the compounds. Our TDDFT study has proved that TDDFT(B3LYP)/6-31+G(d) serves as well-balanced level of theory between computational burden and accuracy in the prediction of the absorption λ_{max} of maleimide-derived heterocycles [30]. The single point TDDFT calculations employed PBE0 [31] and CAM-B3LYP[32] functional as well as B3LYP to obtain the vertical S_0-S_1 excitation energies and their associated oscillator strengths. Solvent effects of ethanol were considered using two PCM methods, non-equilibrium linear response formulation (LR-PCM) [33] and its state-specific variant (SS-PCM) [34]. Complete Active Space Self Consistent Field CASSCF(10e,10o)/ANO-L and Multi-State second order perturbation to CAS MS-CASPT2(10e,10o)/ANO-L calculations were carried out to quantitatively evaluate the λ_{max}.

For the crystalline phase of **7a** and **8a** in the S_0 state, ONIOM and FMO-TDDFT [35] calculations were employed to estimate the absorption λ_{max} under the packing influence. The cluster models were extracted from the crystallographic data shown in the Table S-1,

containing 32 molecules for **7a** and 30 molecules for **8a**, respectively within 10 Å apart from the center of mass of the central molecule, as presented in the Figure 2. The X-ray crystallographic analysis for **8a** provided the uncertainty for the pyrrolindino ring position (two structures with equally partial occupancies), therefore the equally averaged geometrical data was adopted. ONIOM(TDDFT:PM3) (TDDFT for the sole central molecule:PM3 for the surrounding lattice molecules) and FMO-TDDFT calculations were applied to the cluster models. FMO-TDDFT calculations employed 6-31G(d) throughout the present study since the more extended basis set larger than 6-31+G(d) suffered from FMO convergence failure. The intermolecular interactions were estimated within FMO-TDDFT at the two FMO levels; FMO-1 (including only monomer interactions) and FMO-2 (including up to dimer interactions). A correction to Basis Set Superposition Error (BSSE) was not considered for the present calculations. For the S_1 state, cluster models were created through manipulation of the S_0 cluster models, in which the geometries were partially optimized by TDDFT(B3LYP)/6-31+G(d) only for the central one molecule with the surrounding lattice molecules fixed in S_0 state geometry treated by PM3 level, i.e., two-layer ONIOM (TD(B3LYP)/6-31+G(d): PM3). The model has been already studied as a `frozen-molecule approximation` [36]. The partial geometry optimization with the surrounding PM3 regions fixed has been rationalized by Shuai et al using QM/MM model for 3-cyano-2-phenyl-Z-NH-indole cluster models [37]. Single point FMO-TDDFT calculations were carried out for the ONIOM-optimized geometry to estimate the emission λ_{max}.

The DFT, TDDFT and ONIOM calculations were performed by means of Gaussian09 [38], FMO-TDDFT calculations by GAMESS [39], CASSCF and MS-CASPT2 calculations by MOLCAS [40], respectively.

4. Results and discussion

4.1 Absorption spectra of **3, 5, 6**: TDDFT assessment

To verify the applicability of TDDFT, the first intense absorption maxima of compounds **3, 5, 6** series were computed and the results were shown in Table 4. The S_0-S_1 vertical excitations are overwhelmingly described by HOMO-LUMO excitations for all the compounds. The computed λ_{max} show fair coincidence with the experiments in ethanol with around 30 nm deviations, excluding **3k** which is not sufficiently soluble. In comparison of **3** with **5**, the hypsochromic shifts invoked by the introduction of pyrroloindolino group were well reproduced at the present TDDFT level.

4.2 Absorption spectra of **7a** and **8a** both in ethanol and in crystalline phase: ONIOM and FMO-TDDFT calculations

Tables 5 and 6 shows the evolution of absorption λ_{max} of **7a** and **8a** at the series of computational levels.

In vacuo, λ_{max} of **7a** and **8a** show fairly quantitative agreements with experiments at both TDDFT and MS-CASPT2 levels, using the geometries extracted from crystalline state. CASSCF gave substantial λ_{max} over-evaluation owing to the lack of dynamic electron correlation. MS-CASPT2 adequately corrected the CASSCF results toward right prediction. TDDFT using B3LYP functional showed that 6-31+G(d,p) have a qualitative accuracy with its deviation from that of 6-311G++(3df,2dp) only 4 nm for **7a**. That means the compact 6-31+G(d,p) basis set can ensure the quantitative accuracies in the present study. The computed λ_{max} showed a hypsochromic shift in the order of B3LYP<PBE0<CAM-B3LYP; the trend agrees with the XC-functional performances generally established [41].

In ethanol, the two PCM schemes, LR-PCM and SS-PCM, were tested to estimate the solvent effect on the λ_{max}. For **7a**, LR-PCM invoked an apparent blue-shift by 10 nm while SS-PCM give virtually no shift (1 nm), using TD(B3LYP)/6-31+G(d). The same trend was observed for **8a**. The results point out that SS-PCM, which can treat the excited state more flexibly adapted to the excited state than LR-PCM and assumes more accurate results, elucidated the minor role of ethanol exerted on the λ_{max} at PCM level. The PCM solvent effect on MS-CASPT2 works hypsochromically by up to 32 nm. The best agreement with experiments among the solvent-considered calculations were obtained by SS-PCM-TD(B3LYP)/6-31+G(d,p) for **7a** (12 nm deviation) and by vac-MS-CASPT2(10e,10o)/ANO-L for **8a** (1 nm deviation), respectively.

In the crystalline states, head-to-tail pairs are stacked for both **7a** and **8a** (dimer-1) with an interplanar distance over 4 Å, which imply that strong π–π interactions are not invoked but modest dipole-dipole interactions induced instead in the stacking direction as illustrated in Figure 3 and 4. On the other hand, the shortest O-H distance between the parallel adjacent molecules is 2.59 Å (**7a**) and 2.39 Å (**8a**) (dimer-2), respectively, which means substantial hydrogen bond interactions were invoked. The hydrogen pairing caused bathochromic shifts of 40 nm (**7a**) and 14 nm (**8a**) at the TD(B3LYP)/6-31G(d) level. The HOMO-1,HOMO, LUMO and LUMO+1 of **7a** dimer-2 are localized on each monomers, as shown in Figure 5. The S_0-S_1 oscillator strength of the dimer-2 was larger (0.336: **7a**) than monomer (0.204: **7a**) because the pairwise local excitations (HOMO-1 to LUMO, HOMO to LUMO+1)

are almost equally superimposed and enhanced in the dimer-2 S_1 state. The calculated dipole moments of the monomers were directed from the central pyridine ring toward the phenyl ring, with the strength of 14.4 (**7a**) and 13.2 (**8a**) debye, respectively.

The two layer ONIOM(TDDFT:PM3) results gave negligible shifts to λ_{max}, which implys the electrostatic interactions across the two layers may not be properly treated at semiempirical MO levels. In comparison with the hypsochromic shift obtained by FMO1-TDDFT which include only one-body interactions, point charge approximation to the surrounding PM3 shells (Mulliken charges on the surrounding molecules treated by PM3 are nullified) did not properly describe the coulombic interactions between DFT and PM3 regions. ONIOM-optimized geometrical distortions are compared with X-ray crystallographic data in Table 7, which illustrate the inter-ring C-C bond lengths and the relevant torsion angles in good agreement within ca. 0.01 Å and 1.5 degree deviations for **7a**, respectively. **8a** shows modest deviation of the twist angles with ca. 6 degrees between the ONIOM-optimized and X-ray angles, which imply that **8a** in the solid state is influenced by crystal field which make it favorable to stay in more planar conformation.

The importance of appropriate treatment of surrounding molecules in solid state is indicated by the FMO-TDDFT results for the same cluster models, as presented in Table 8. The FMO1-TDDFT invoked the blue shift by 11 for **7a** and 23 nm for **8a**, respectively, in comparison with the in-vacuo results. FMO2-TDDFT, which consider up to pairwise 2-body interactions with the central monomer, invoked inverse adjustment by 5 nm from FMO1-TDDFT to predict λ_{max} at 326 nm. The bathochromic shift in FMO2-TDDFT was presumably derived from the same behavior between monomer and dimer with a 9 nm red shift. Provided that the 6 nm gap between TD(B3LYP)/6-31G(d) and TD(B3LYP)/ 6-311++G(3df,2dp) can be extrapolated to the case of FMO2-TDDFT, the most sophisticated strategy in the present TDDFT study FMO2-TDDFT/6-311++G(3df,2dp) would give 332 nm with only 2 nm deviation form the experiment 334 nm, in excellent agreement for **7a**. Still, the small blue shift was experimentally observed for **7a** in solid (334 nm) in comparison with in ethanol (350 nm) while the substantial red shift was noted for **8a** between in solid (394 nm) and in ethanol (310 nm). The inconsistency for **8a** with substantial gap between theory and experiment is not satisfactorily explainable at the present computational levels.

The individual contributions from the FMO2 pairs to λ_{max} were examined in detail, as shown in Table S-2. For **7a**, the largest contribution to excitation energy is derived from the pair interaction with the 14^{th} molecule giving a 0.040 eV hypsochromic shift, followed by the

next largest contribution from 12th molecule with -0.033 eV, followed by 11th with -0.018 eV. The 14th molecule is aligned with 1st in an anti-parallel fashion while 12th and 11th is interconnected with 1st via a hydrogen bond. The bathochromic shift induced by an intermolecular hydrogen bond has been already reported by a FMO-TDDFT study of quinacridone crystals [42]. The resulting excitation energy of **7a** was calculated to be 326 nm, with 6 nm bathochromic shift from 320 nm at FMO1 level. The modest contributions from the pair interactions with 6 nm red shift were observed for **8a** as well.

4.3 Emission spectra of **3f**

Table 9 illustrates the solvent effect on the first intense emission λ_{max} computationally assessed for **3f**, which exhibited highest fluorescence quantum yield 0.03 among the present molecules in ethanol. LR-PCM calculations provided small λ_{max} shifts within 10 nm irrespective of the XC-functionals employed, while SS-PCM gave substantial bathochromic shifts by over 30 nm. SS-PCM-TD(B3LYP)/6-31+G(d) gave the best coincidence with the experiment with 38 nm deviation. The result of MS-CASPT2 worsened the coincidence even including the solvent effect, where PCM solvent effect might excessively destabilize the S_1 state, leading to the widened S_1-S_0 vertical gap. This irregularity of PCM could indicate the limitation of the present PCM implementation combined with MS-CASPT2.

A substantially bathochromic shift invoked by the packing effect was observed in the solid state compared to that in ethanol by 50 nm (Table 1). Unfortunately we failed to obtain the crystals so we could not computationally estimate the emission λ_{max} using the crystalline structure. The packing effects on emission λ_{max} are discussed in the following subsection 4.4 for **7a** and **8a** of which crystal structures are available.

4.4 Emission spectra of **7a** and **8a** both in ethanol and in solid state: ONIOM and FMO-TDDFT calculations

As shown in Table 7, the key C4-C7 bond length of **7a** becomes shortened by 0.04 Å in comparison with the optimized geometries in vacuo in the S_0 and the S_1 states. The associated inter-ring twisting angle between the central pyridine ring and the phenyl counterpart was restored by 25 degrees in the S_1 state. This indicates that the electronic resonance between the C4-C7 bond is somewhat restored in the S_1 state. Such resonance restoration was computed for **8a** as well. The geometrical distortions between in vacuo-optimized and ONIOM-optimized structures are quite small in the S_1 state as in the S_0 state. The ONIOM-optimized structures, interestingly, showed that the skeletal twisting angles become larger by 14 degrees both for **7a**

and **8a**. It is unclear whether the enhanced distortion is caused by the surrounding lattice molecules or simply the irregularity of the finite cluster model.

Table 10 shows the computed emission λ_{max} evolution. In vacuo, the emission λ_{max} dependency on the basis set shows the trend similar to those of the UV-vis λ_{max}, namely, the bathochromic shift for the two molecules. The best coincidence was obtained using B3LYP among the three XC-fuctionals with the experimental emission λ_{max} in the solid state. As in the case of the S_0 state, CASSCF λ_{max} was adequately corrected by MS-CASPT2, giving 418 nm with 30 nm deviation from TD(B3LYP)/6-31+G(d) for **7a**. The calculated dipole moment vector in the S_1 state possess the strength of 11.8 (**7a**) and 10.6 (**8a**) debye respectively, directing from the central pyridine ring toward phenyl ring, as in the S_0 state.

The ONIOM emission λ_{max} were predicted at 421 (435) nm for **7a** (**8a**) at TD(B3LYP)/6-31G(d) level, 25 (28) nm blue shift than the TDDFT results in vacuo, respectively. Considering the negligible ONIOM effect on the S_0 state where quite small absorption λ_{max} shifts were invoked, the substantial emission red shifts were caused by the considerable geometrical distortions in the S_1 state which exerted on the emission center molecule embedded in the surrounding molecules as a result of the geometry optimizations.

As shown in Table 8, FMO-TDDFT λ_{max} on the ONIOM-geometries exhibited further hypsochromic shift from the ONIOM-TDDFT results; for **7a** 403 nm by FMO-1 and 415 nm by FMO-2, and for **8a** 392 nm by FMO-1 and 397 nm by FMO-2, respectively. The dimer interactions between the emission center and the surrounding molecules considered in FMO-2 adjusted the λ_{max} toward bathochromic directions, as in the case in the S_0 state. The λ_{max} coincidence between the experiments and calculations are much worse than the case of the S_0 state in which almost perfect coincidence was obtained at FMO2-TDDFT level. The substantial λ_{max} gap of 51 (87) nm for **7a** (**8a**) remains even at the FMO2-TDDFT level, respectively. Considering the good coincidence of MS-CASPT2 and FMO2-TDDFT, the substantial gap might be attributed not only to the computational accuracies, but to the large displacement between FC-S_1 and the S_1 minima; the emissive S_1 state is supposedly located not at the FC-S_1 point or nearby but at the point far from FC-S_1 as result of geometrical relaxations. The precise S_1 energy surface exploration, however, goes beyond the present study.

The FMO2-TDDFT individual pair contributions to λ_{max} shift are shown in Table S-2. For **7a**, the largest contribution to the FMO-1 λ_{max} (403 nm) come from the interaction with the 11^{th} molecule of -0.027 eV hypsochromic shift, followed by the next largest contribution with the molecule 10^{th} of -0.023 eV followed by 6^{th} of 0.015 eV, leading to the resulting

FMO-2 λ_{max} calculated to be 415 nm of 12 nm bathochromic shift. The two blue-shift-causing pairs were interconnected with the center molecule through hydrogen bonds while the red-shift-causing pair was stacked in an anti-parallel fashion, as show in Figure 6. The modest contributions from the pair interactions with 5 nm red shift was observed for **8a** as well by introduction of the two-body interaction corrections into FMO-1, as shown in Table 8.

The present study ignored electrostatic interactions from infinite distances in the crystalline state; the crystal field effect can contribute at the same magnitude as structure deformation and intermolecular interactions to excitation energy [42]. The cluster size dependency, new XC-functionals to treat dispersion interactions, higher order correction beyond two-body interactions in FMO-TDDFT, the adequacy of the 'frozen-molecule approximation'[36] will be studied in due course.

5. Conclusion

In summary, a joint experimental and computational study of UV-vis and fluorescence first intense maxima of the new 2(*1H*)-pyridone derivatives was presented and discussed in vacuo, in solution and in the solid state. The UV-vis peaks of the compounds appeared between 310-449 nm in ethanol. Some of them showed modest fluorescence in solid state in the range of 431-564 nm but quite weak or no fluorescence in solution. The TDDFT and MS-CASPT2 calculations including solvent effects reveal that the two PCM methodologies, LR-PCM and SS-PCM, affect the UV-vis and emission peak shifts in a quantitatively different way. The UV-vis and fluorescence peaks of the two representative compounds (**7a**, **8a**) in the solid state were examined in detail by means of ONIOM and FMO-TDDFT methods, in order to analyze an interplay between geometrical distortions and intermolecular interactions. For the absorption λmax, intermolecular hydrogen bonds considered by FMO2 invoked red shifts whereas non-hydrogen bond interactions induced blue shift, giving bathochromic shift in total from FMO1. The overall packing effects treated by FMO2-TDDFT invoked blue shift of 11 nm from λ_{max} of **7a** in vacuo, also 23 nm blue shift from that of **8a**. The ONIOM influence on the absorption λ_{max} derived from the surrounding molecules is quite marginal within 1 nm shift. The minor influence of ONIOM on the absorption λ_{max} indicates that the substantial ONIOM influence on the emission λ_{max} comes from the geometrical deviations in the S_1 state by the surrounding molecules, not from the direct perturbation to the electronic structure of the emissive molecule.

Acknowledgement

One of the authors (Y.S.) thanks to Dr. Takeshi

Ishikawa of Nagasaki University for his helpful discussions on the interpretations of ONIOM and FMO-TDDFT calculations. This study was financially supported in part by Grants-in-Aid for Scientific Research (C) (No. 24550058, Y.S.) from Japan Society for the Promotion of Science.

References

[1] Shirai K, Matsuoka M, Fukunishi K. New syntheses and solid state fluorescence of azomethine dyes derived from diaminomaleonitrile and 2,5-diamino-3,6-dicyanopyrazine. Dyes and Pigments 2000; 47: 107-115. and references therein

[2] He Z, Kan C.W., Ho C.L., Wong W.Y., Chui C.H., Tong K.L., So S.K., Lee T.H., Leung L.M., Lin Z. Light-emitting dyes derived from bifunctional chromophores of diarylamine and oxadiazole: Synthesis, crystal structure, photophysics and electroluminescence, Dyes and Pigments, 2011; 88:333-343.

[3] Tang K-C., Chang M-J, Lin T-Y, Pan H-A., Fang T-C, Chen K-Y, Hung W-Y, Hsu Y-H, Chou T-P., Fine Tuning the Energetics of Excited-State Intramolecular Proton Transfer (ESIPT): White Light Generation in A Single ESIPT System. J. Am. Chem. Soc. 2011; 133,:17738-17745

[4] Zhang Q, Li J, Shizu K, Huang S, Hirata S, Miyazaki H, Adachi C, Design of Efficient Thermally Activated Delayed Fluorescence Materials for Pure Blue Organic Light Emitting Diodes. J. Am. Chem. Soc. 2012;134:14706-14709

[5] Li J., Duan Y, Li Q. Novel thieno-[3,4-b]-pyrazine derivatives for non-doped red organic light-emitting diodes. Dyes and Pigments, 2013; 96: 391-396.

[6] Park S-Y, Ebihara M, Kuroda Y, Funabiki K, Matsui M. The relationship between solid-state fluorescence intensity and molecular packing of coumarin dyes. Dyes and Pigments 2009; 82: 258-267.

[7] An B-K, Kwon S-K, Jung, S-D, Park S-Y. Enhanced emission and its switching in fluorescent organic nanoparticles. J. Am. Chem. Soc. 2002; 124: 14410−14415.

[8] Feng X, Tong B, Shen J, Shi J, Han T, Chen L, Zhi J, Lu P, Ma Y, Dong Y. Aggregation-Induced Emission Enhancement of Aryl-Substituted Pyrrole Derivatives. J. Phys. Chem. B 2010;114:16731-16736.

[9] Xie Y-Z, Shan G-G, Li P, Zhou Z-Y, Su Z-M. A novel class of Zn(II) Schiff base complexes with aggregation-induced emission enhancement (AIEE) properties: Synthesis, characterization and photophysical/electrochemical properties. Dyes and Pigments, 2013;96:467-474.

[10] Kitaura K, Ikeo E, Asada T, Nakano T, Uebayasi M. Fragment molecular orbital method: an approximate computational method for large molecules. Chem. Phys. Lett. 1999; 313:701-706.

[11] Kitaura K, Fedrov D.G. Eds. The Fragment Molecular Orbital Method, CRC press, New York, 2009.

[12] Canuto S, Sabin J.R. Eds, Combining Quantum Mechanics and Molecular Mechanics. Some Recent Progresses in QM/MM Methods, in Advances in Quantum Chemistry Volume 59, 2011,Academic press, and references therein

[13] Dapprich S, Komáromi I, Byun KS, Morokuma K, Frisch M.J, A New ONIOM Implementation in Gaussian 98. 1. The Calculation of Energies, Gradients and Vibrational Frequencies and Electric Field Derivatives. J. Mol. Struct. (Theochem). 1999; 462:1-21.

[14] Kaes C, Katz A, Hosseini MW. Bipyridine: The Most Widely Used Ligand. A Review of Molecules Comprising at Least Two 2,2‘-Bipyridine Units. Chem. Rev. 2000;100:3553-3590. and references therein

[15] Chen CH, Tang CW, Shi J, Klubeck .P, Recent developments in the synthesis of red dopants for Alq_3 hosted electroluminescence. Thin Solid Films 2000;363:327-331. and references therein

[16] Mizuyama N, Murakami Y, Kohra S, Ueda K, Hiraoka K, Nagaoka J, Takahashi K, Shigemitsu Y, Tominaga Y. Synthesis and Fluorescence of 2H-Pyrone Derivatives for Organic Light-emitting Diodes (OLED) . Journal of Heterocyclic Chemistry 2007;44,:115-132.

[17] Mizuyama N, Tominaga Y, Kohra S, Ueda K, Hirayama S, Shigemitsu Y. Synthesis and Steady-State Spectroscopic Study of 5-Aryl-2,2'-bipyridyls. New Fluorescent Compounds in Solid State. Bull. Chem. Soc. Jpn, 2006;79, 602-611.

[18] Held A, Champagne BB, Pratt DW. Inertial axis reorientation in the S_1 <- S_0 electronic transition of 2-pyridone. A rotational Duschinsky effect. Structural and dynamical consequences. J.Chem.Phys. 1991;5:8732-8743.

[19] Matsuda Y, Ebata T, Mikami N. Vibrational spectroscopy of 2-pyridone and its clusters in supersonic jets : Structures of the clusters as revealed by characteristic shifts of the NH and C=0 bands. J.Chem.Phys., 1999; 110:8397-8407.

[20] Flakus HT, Tyl A, Maslankiewicz A. Electron-Induced Phase Transition in Hydrogen-Bonded Solid-State 2-Pyridone. J.Phys.Chem.A, 2011;115:1027-1038.

[21] Borst DR, Roscioli JR, Pratt DW, Florio GM, Zwier TS, Muller A, Leutwyler S. Hydrogen bonding and tunneling in the 2-pyridone·2-hydroxypyridine dimer. Effect of electronic excitation. Chem. Phys.2002; 283:341-354.

[22] Casinovi CG, Grandolini G, Mercantini R, Oddo N, Olivieri R, Tonolo A. A new antibiotic produced by a strain of Aspergillus flavipes. Tetrahedron Lett. 1968;3175-3178.

[23] Datta A, Ila H, Junjappa H. Reformatsky reaction on α-oxoketene dithioacetals; Synthesis of substituted

and fused ethyl-2-hydroxy-6-methylthiobenzoates, 6-methylthio-3(1H)pyridones and 6-methyl-thiopyran-2-one derivatives. J. Org. Chem. 1990;55:5589-5594.

[24] Tominaga Y, Kawabe M, Hosomi A. Synthesis of 4-methylthio-2(1H)-pyridone derivatives using ketene dithioacetals. J. Heterocycl. Chem. 1987;24:1327-1331. and references therein

[25] Tominaga Y, Ushirogouchi A, Matsuda Y, Synthesis and reaction of 6-substituted 3-methoxycarbonyl-4-methylthio-2H-pyran-2-one derivatives. J. Heterocycl. Chem., 1987;24:1557-1567. and references therein

[26] Dieter RK. α-Oxo ketene dithioacetals and related compounds: versatile three-carbon synthons. Tetrahedron, 1986;42:3029-3096.

[27] Patsenker LD, Artyukhova YY. Molecular structure and spectral properties of thionaphthalimides. J. Mol. Struct., 2003;655:311-320.

[28] Becke, A. Density‐functional thermochemistry. III. The role of exact exchange. J.Chem.Phys., 1993;98:5648-5652

[29] Lee C, Yang W, Parr RG. Development of the Colle-Salvetti Correlation-Energy Formula into a Functional of the Electron DensityPhys.Rev. B 1998;37:785-789.

[30] Shigemitsu Y, Komiya K, Mizuyama N, Tominaga Y. TD-DFT investigation on the electronic spectra of novel N -methylmaleimides linked with indolizine ring system. J. Mol.Struct. (THEOCHEM), 2008; 855:92-101.

[31] Adamo C, Barone V. Toward reliable density functional methods without adjustable parameters: The PBE0 model. J. Chem. Phys. 1999;110 :6158-69.

[32] Yanai T, Tew D, Handy N. A new hybrid exchange-correlation functional using the Coulomb-attenuating method (CAM-B3LYP). Chem. Phys. Lett. 2004;393: 51-57.

[33] Cossi M, Barone V. Time-dependent density functional theory for molecules in liquid solutions. J.Chem.Phys. 2001; 115:4708-4718.

[34] Improta R, Barone V, Scalmani G, Frisch MJ. A state-specific polarizable continuum model time dependent density functional method for excited state calculations in solution. J. Chem. Phys., 2006; 125: 1-9.

[35] Chiba M, Fedorov DG, Kitaura K. Time-dependent density functional theory with the multilayer fragment molecular orbital method. Chem. Phys. Lett. 2007; 444:346-350.

[36] Li M-C, Hayashi M, Lin S-H. Quantum Chemistry Study on Internal Conversion of Diphenyldibenzofulvene in Solid Phase. J.Phys.Chem.A, 2011; 115:14531-14538.

[37] Wu Q, Peng Q, Niu Y, Gao X, Shuai Z. Theoretical insights into the aggregation-induced emission by hydrogen bonding: a QM/MM study. J

Phys Chem A 2012; 116:3881-3888.

[38] Gaussian 09 , Rev. A.2, M. J. Frisch, G. W. Trucks, H. B. Schlegel, G. E. Scuseria, M. A. Robb, J. R. Cheeseman, V. G. Zakrzewski, J. A. Montgomery, Jr., R. E. Stratmann, J. C. Burant, S. Dapprich, J. M. Millam, A. D. Daniels, K. N. Kudin, M. C. Strain, O. Farkas, J. Tomasi, V. Barone, M. Cossi, R. Cammi, B. Mennucci, C. Pomelli, C. Adamo, S. Clifford, J. Ochterski, G. A. Petersson, P. Y. Ayala, Q. Cui, K. Morokuma, D. K. Malick, A. D. Rabuck, K. Raghavachari, J. B. Foresman, J. Cioslowski, J. V. Ortiz, A. G. Baboul, B. B. Stefanov, G. Liu, A. Liashenko, P. Piskorz, I. Komaromi, R. Gomperts, R. L. Martin, D. J. Fox, T. Keith, M. A. Al-Laham, C. Y. Peng, A. Nanayakkara, C. Gonzalez, M. Challacombe, P. M. W. Gill, B. G. Johnson, W. Chen, M. W. Wong, J. L. Andres, M. Head-Gordon, E. S. Replogle and J. A. Pople, Gaussian, Inc., Pittsburgh PA.

[39] GAMESS-US version 2009, Department of Chemistry, Iowa State University, Ames, IA 50011, 2009.

[40] MOLCAS ver.7.4, Lund University, 2008; Aquilante, F.; Vico, L.De.; Ferré, N.; Ghigo, G.; Målmqvist, P.-Å; Neogrády, P.; Pedersen, T.B.; Pitonak, M.; Reiher, M.; Roos, B.O.; Serrano-Andrés, L.; Urban, M.; Veryazov, V.; Lindh, R.

[41] Jacquemin D, Mennucci B, Adamo C. Excited-state calculations with TD-DFT: from benchmarks to simulations in complex environments. Phys. Chem. Chem. Phys., 2011;13,:16987-16998.

[42] Fukunaga H, Fedrov DG, Chiba M, Nii K, Kitaura K. Theoretical Analysis of the Intermolecular Interaction Effects on the Excitation Energy of Organic Pigments:Solid State Quinacridone. J.Phys.Chem.A, 2008;112:10887-10894.

Figure Captions

Fig.1. Synthetic scheme of (3, 5, 6, 7, 8)

Fig.2. ONIOM(DFT:PM3) cluster models of 7a with 32 (upper) and of 8a with 30 molecules (lower). A DFT-treated center molecule surrounded by PM3-treated outer molecules.

Fig.3. 7a monomer (top: an allow indicating a dipole direction), dimer-1 (middle left), dimer-2 (middle right), packing form along a-axis (bottom left), along b-axis (bottom right)

Fig.4. 8a monomer (top: an allow indicating a dipole direction), dimer-1 (middle left), dimer-2 (middle right), packing form along a-axis (bottom left), along b-axis (bottom right)

Fig.5. Near-frontier orbitals of 7a dimer-2. HOMO-1 (upper left), HOMO (upper right), LUMO (lower left), LUMO+1 (lower right).

Fig.6. Representative interacting molecules in 7a cluster model in S0 state. A center molecule (red), 14-th (yellowgreen), 11-th (yellow), 12-th (purple).

Fig.7. Representative interacting molecules in **7a** cluster model in S1 state. A center molecule (red), 6-th (yellowgreen), 10-th (yellow), 11-th (purple).

Fig. 1.

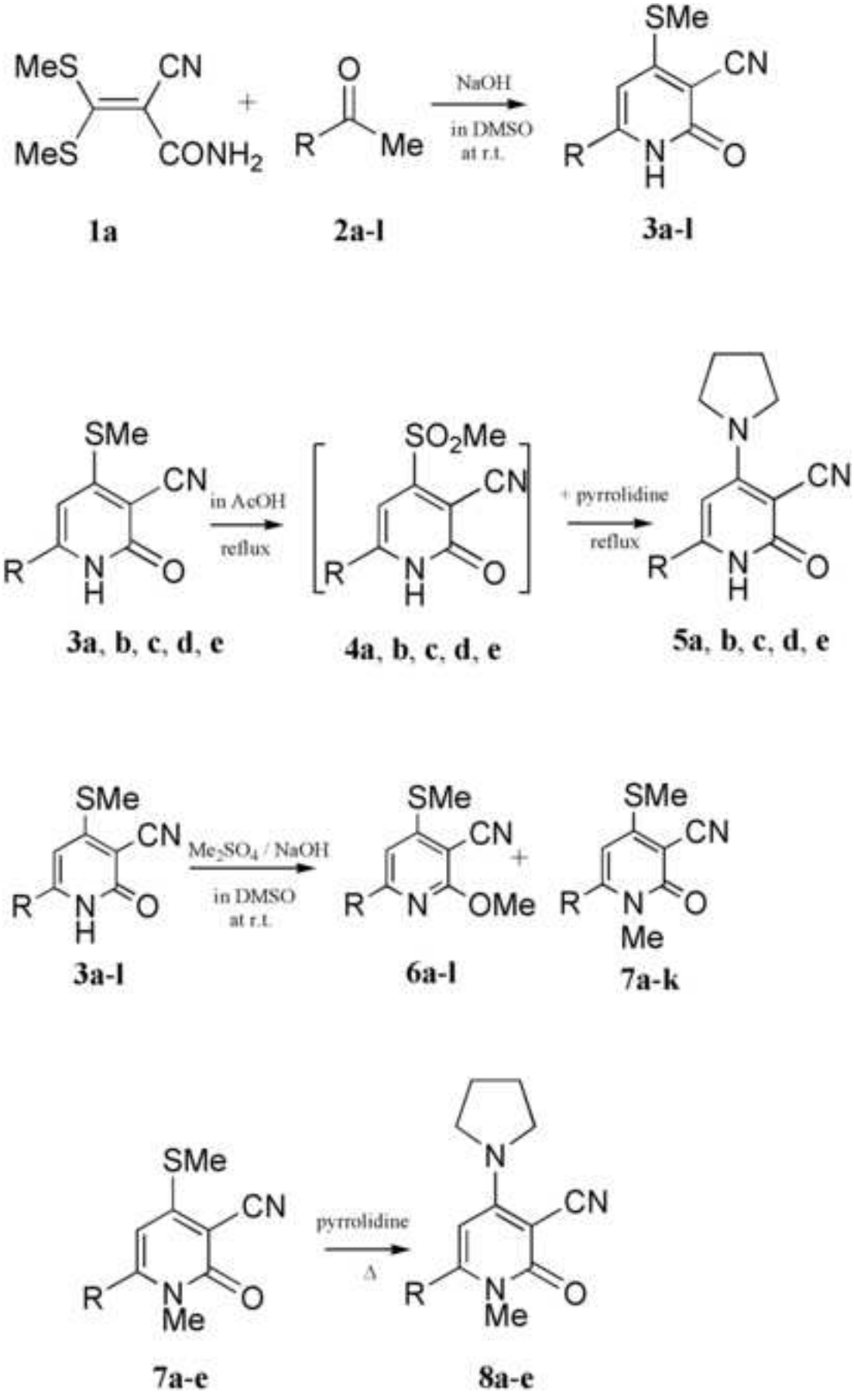

Fig. 1. Synthetic scheme of (3,5,6,7,8)

Fig. 2.

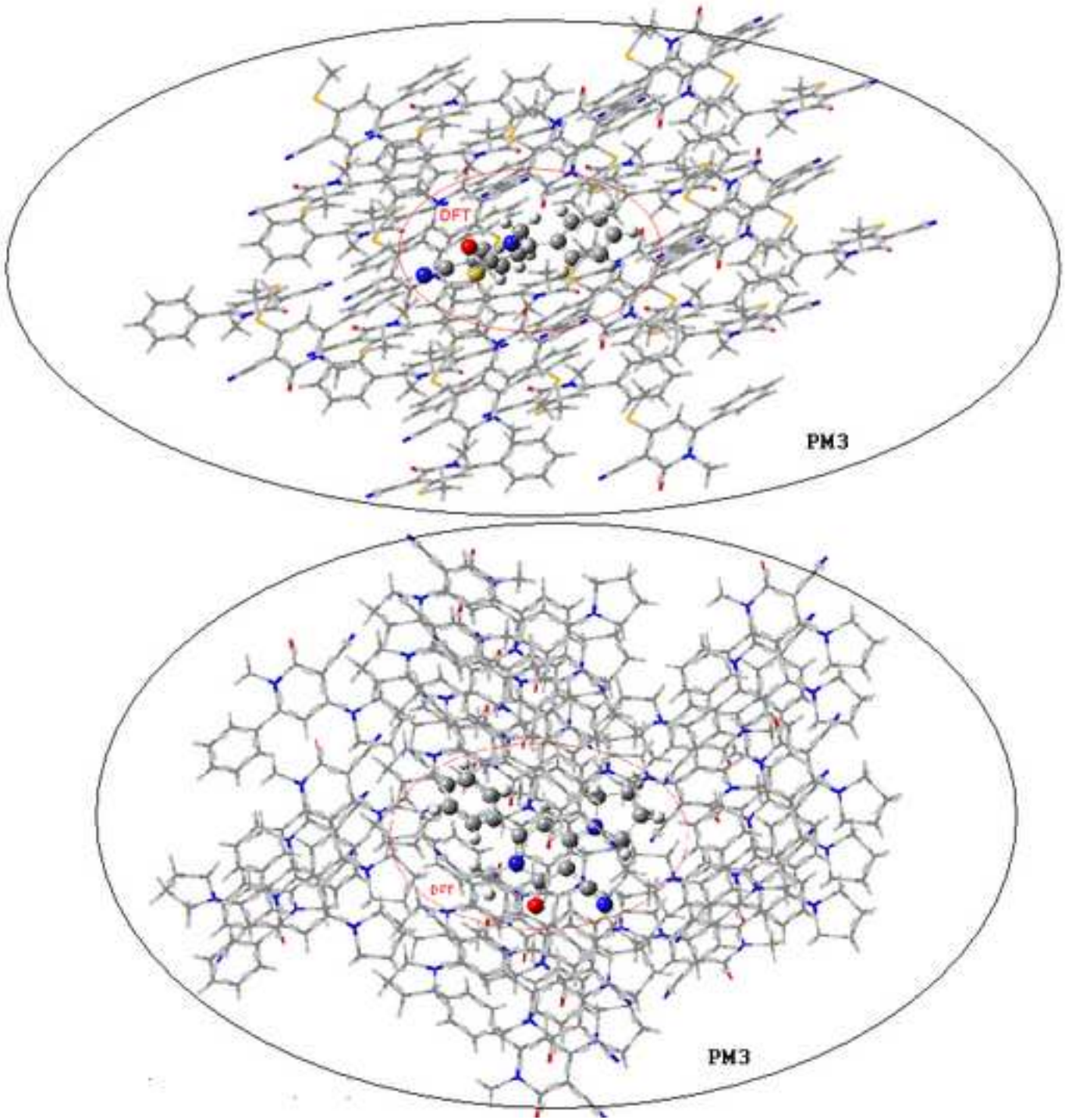

Fig. 3.

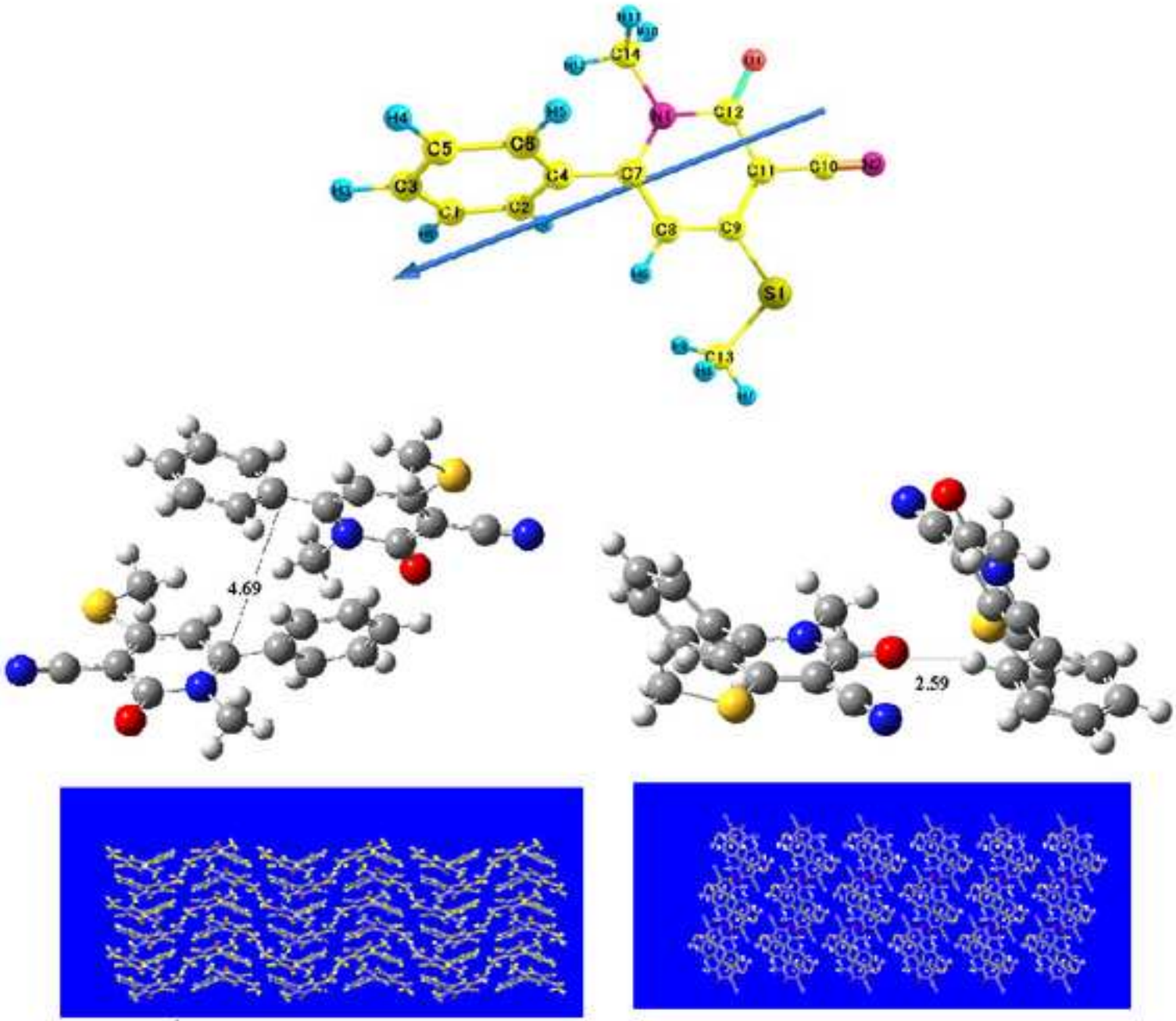

Fig. 4.

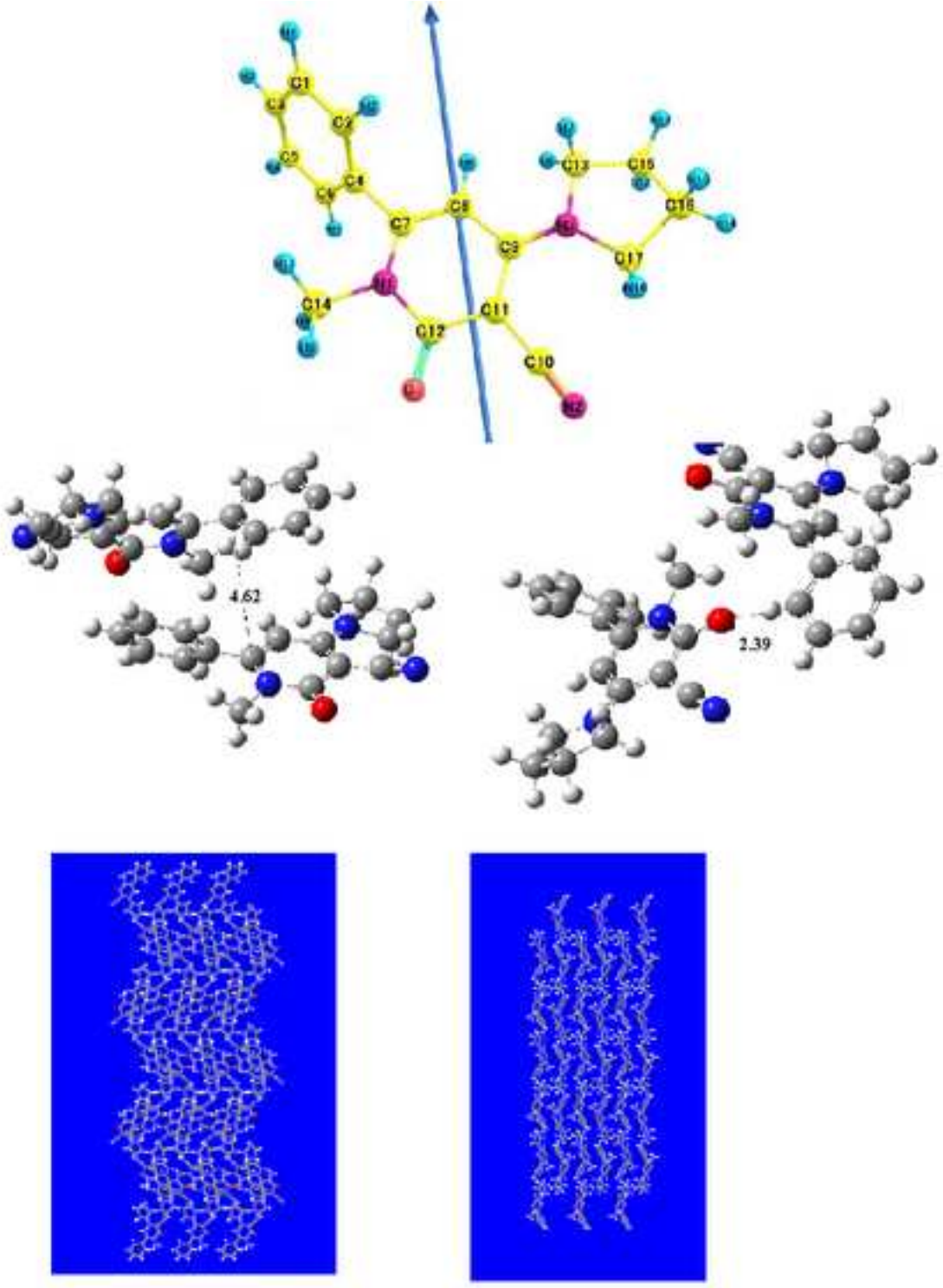

Fig. 5.

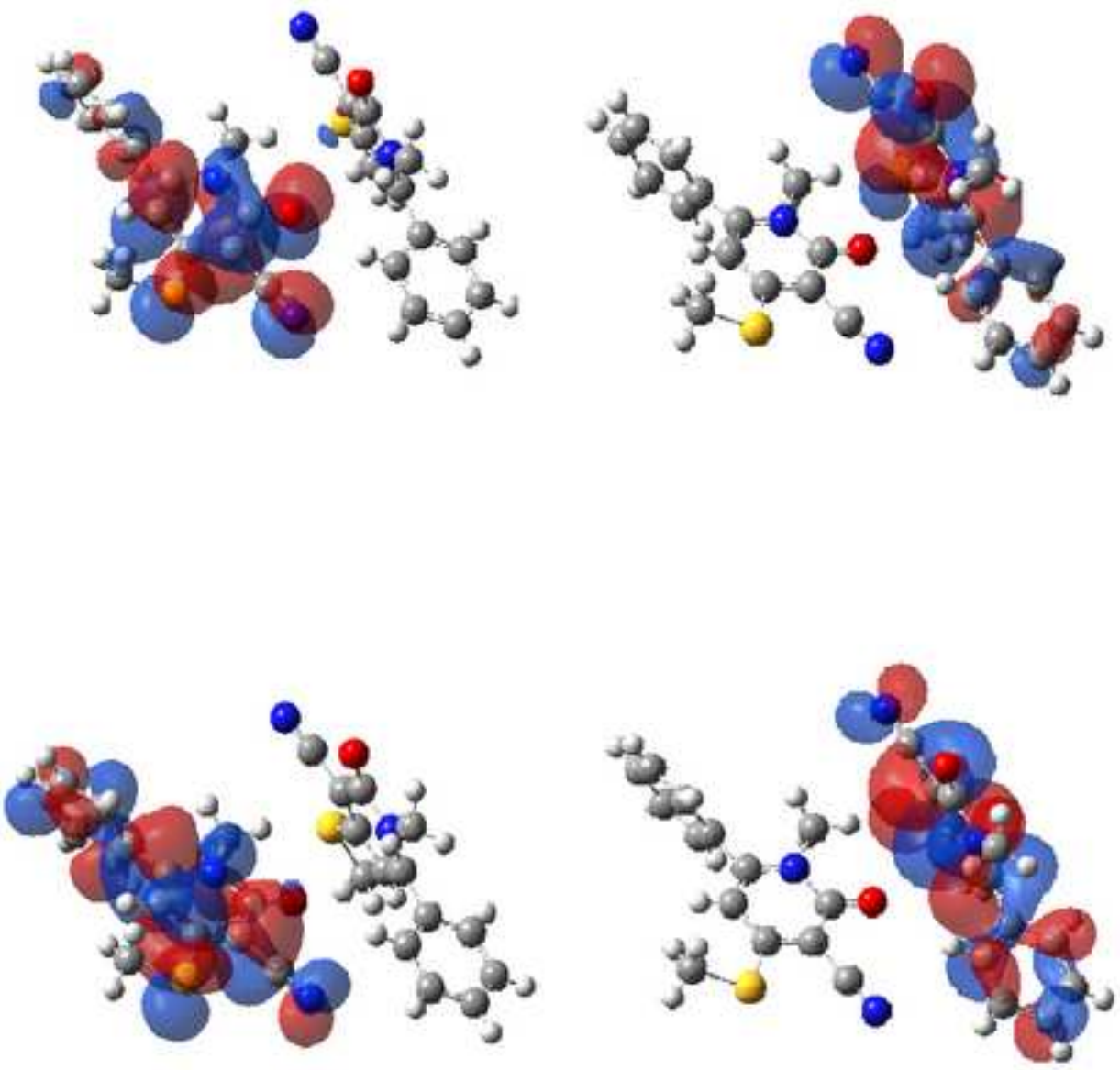

Fig. 6.

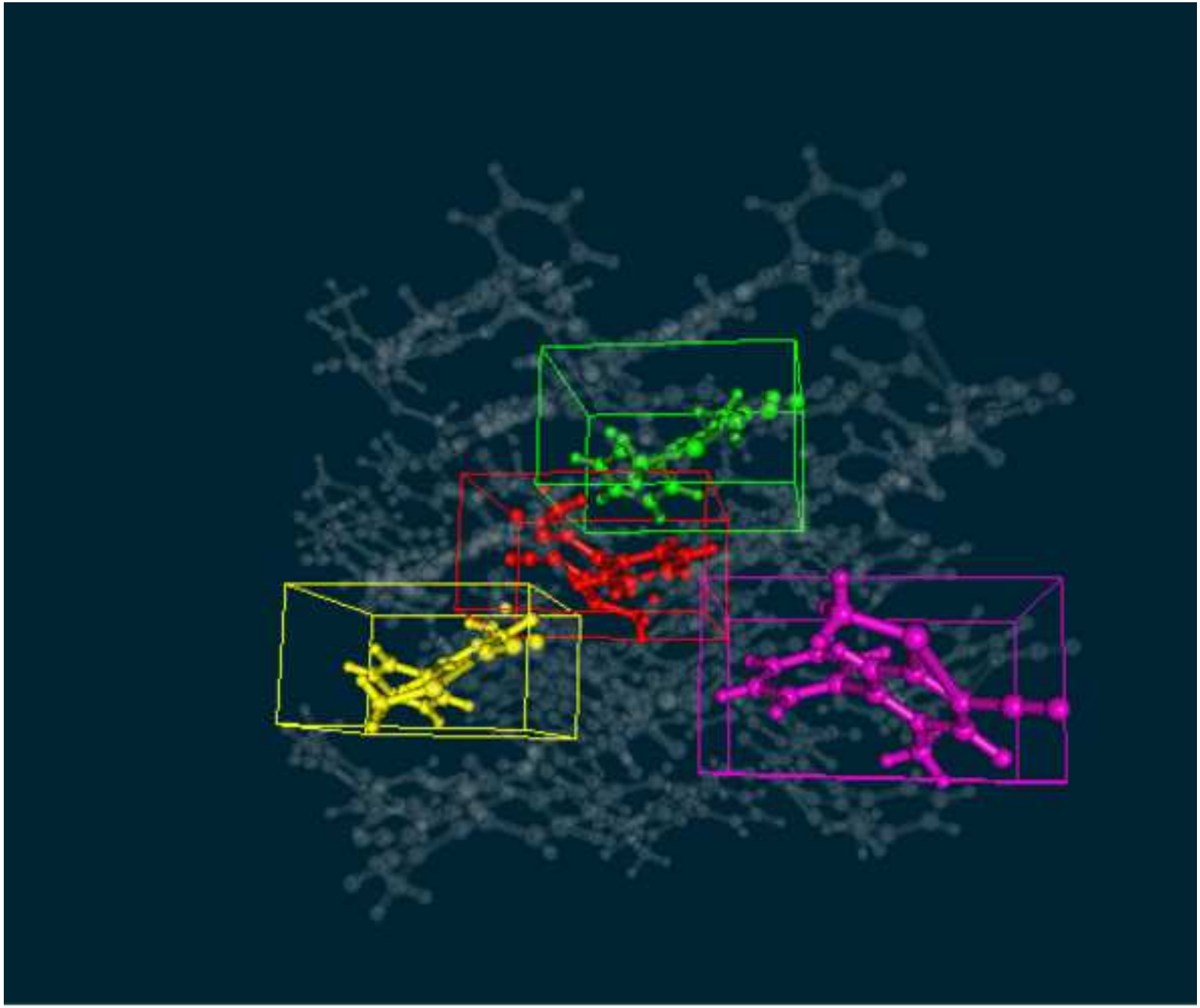

Fig. 7.

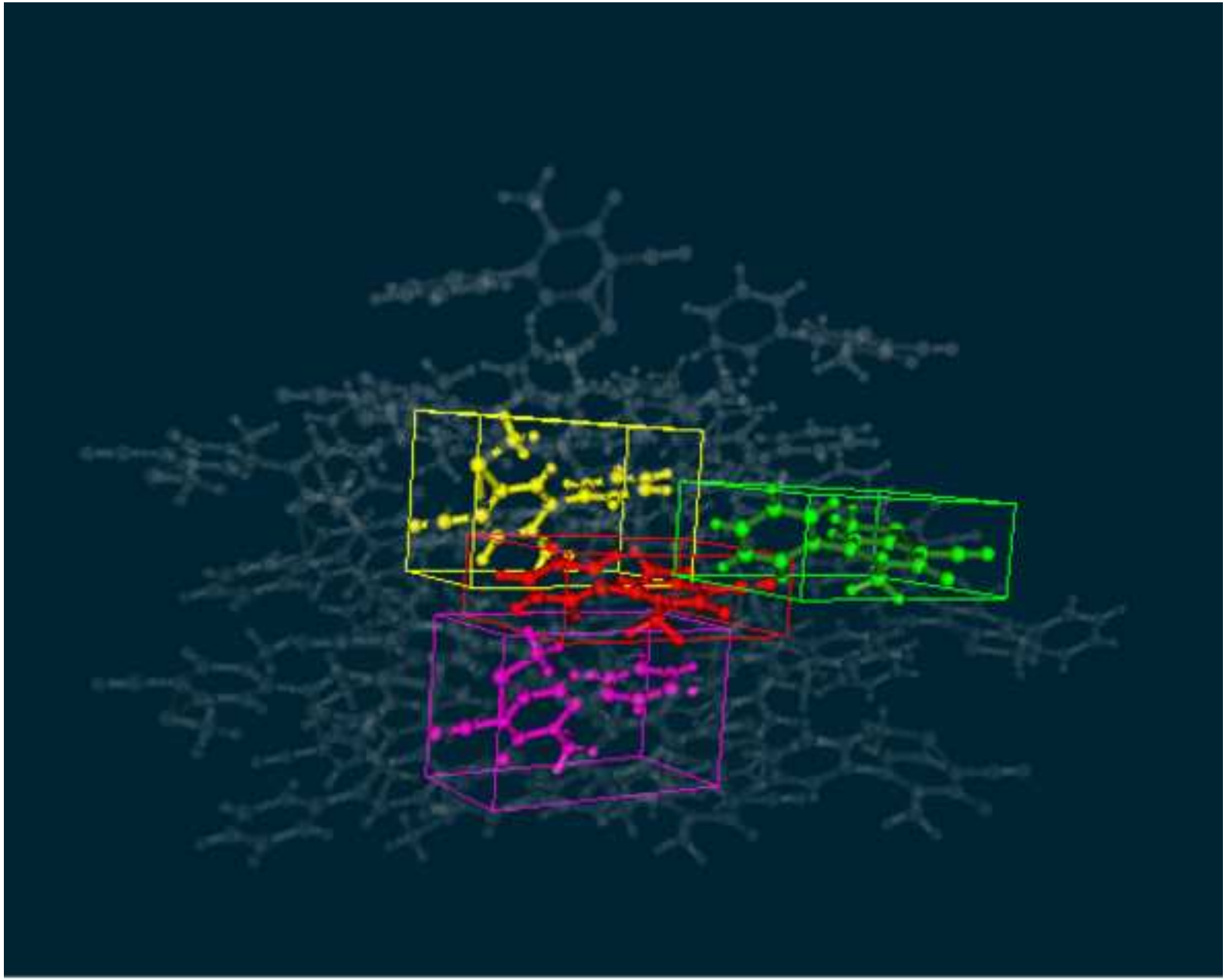

Table 1 UV/vis and fluorescence maxima of **3** and **5**

			UV λmax(log ε)	Fluorescence (EtOH)				Fluorescence (solid)			
No.	position 4	position 6	nm (EtOH)	Ex max(nm)	Em max(nm)	SS[a]	ϕ	Ex max(nm)	Em max(nm)	SS[a]	R.I.[b]
3a	SMe	C_6H_5	356 (4.12)				0.00	346	513	167	0.99
3b	SMe	C_6H_4-OMe(4)	365[c]				0.00	338	496	158	1.28
3c	SMe	C_6H_3-$(OMe)_2$(3,4)	370[c]				0.00	331	506	175	0.92
3d	SMe	C_6H_3-$(OMe)_2$(2,5)	360 (4.12)				0.00	347	476	129	1.22
3e	SMe	C_6H_2-$(OMe)_3$(3,4,5)	364 (4.29)				0.00	345	518	173	0.62
3f	SMe	C_6H_4-NMe_2(4)	410 (4.67)	417	508	91	0.03	340	558	218	1.24
3g	SMe	biphenyl	364[c]				0.00	336	492	156	0.21
3h	SMe	2-pyridyl	366 (3.61)				0.00	350	502	152	0.14
3i	SMe	2-thienyl	375[c]				0.00	339	510	171	0.63
3j	SMe	2-furyl	377 (4.39)				0.00	352	518	166	0.33
3k	SMe	6-styryl	504[c]				0.00	335	560	225	0.23
3l	SMe	2-(4-dimethylaminophenyl)vinyl	449 (4.12)				0.00	327	564	237	0.04
5a	pyrrolidino	C_6H_5	317 (3.85)				0.00	350	453	103	0.42
5b	pyrrolidino	C_6H_4-OMe(4)	324 (4.48)				0.00	350	452	102	3.84
5c	pyrrolidino	C_6H_3-$(OMe)_2$(3,4)	386 (3.95)				0.00	344	497	153	0.71
5d	pyrrolidino	2-pyridyl	335 (4.15)				0.00	346	457	111	0.56
5e	pyrrolidino	2-furyl	335 (4.21)				0.00	349	478	129	0.05

[a] Stoke's Shift = Em max(nm) - Ex max(nm).

[b] Relative intensity of fluorescence in solid state, using Alq_3 as a standard.

[c] insufficient solubility.

Table 2 UV/vis and fluorescence maxima of **6** and **7**

			UV λmax(log ε)	Fluorescence (EtOH)				Fluorescence (solid)			
No.	position 4	position 6	nm (EtOH)	Ex max(nm)	Em max(nm)	SS[a]	ϕ	Ex max(nm)	Em max(nm)	SS[a]	R.I.[b]
6a	SMe	C_6H_5	310 (4.33)	268	623	355	0.01>	356	438	82	1.34
6b	SMe	C_6H_4-OMe(4)	336 (4.62)				0.00	350	452	102	1.83
6c	SMe	C_6H_3-$(OMe)_2$(3,4)	344 (4.43)	246	430	184	0.01>	352	441	89	1.12
6d	SMe	C_6H_3-$(OMe)_2$(2,5)	350 (4.08)	231	460	229	0.01>	343	442	99	0.18
6e	SMe	C_6H_2-$(OMe)_3$(3,4,5)	333 (4.18)	334	450	116	0.01>	341	473	132	0.91
6f	SMe	C_6H_4-NMe_2(4)	383 (4.72)	386	488	102	0.01	341	488	147	1.13
6g	SMe	biphenyl	333 (4.59)	336	426	90	0.01	353	449	96	0.19
6h	SMe	2-pyridyl	313 (4.34)				0.00	344	447	103	0.10
6j	SMe	2-furyl	343 (4.30)	344	426	82	0.01>	344	495	151	1.61
6l	SMe	2-(4-dimethylaminophenyl)vinyl	450 (4.25)				0.00	300	488	188	0.02
7a	SMe	C_6H_5	350 (4.15)				0.00	334	492	158	0.94
7b	SMe	C_6H_4-OMe(4)	350 (4.77)				0.00	355	443	88	3.90
7c	SMe	C_6H_3-$(OMe)_2$(3,4)	350 (4.08)				0.00	344	434	90	1.62
7d	SMe	C_6H_3-$(OMe)_2$(2,5)	350 (4.06)				0.00	346	431	85	0.18
7e	SMe	C_6H_2-$(OMe)_3$(3,4,5)	350 (4.09)				0.00	349	456	107	0.85
7f	SMe	C_6H_4-NMe_2(4)	388 (4.63)	257	454	197	0.01>	340	533	193	1.08
7j	SMe	2-furyl	374 (5.14)				0.00	340	488	148	2.01
7k	SMe	6-styryl	375 (4.59)				0.00	352	518	166	1.65

[a] Stoke's Shift = Em max(nm) - Ex max(nm).

[b] Relative intensity of fluorescence in solid state, using Alq_3 as a standard.

[c] insufficient solubility.

Table 3 UV/vis and fluorescence maxima of **8**

			UV λmax(log ε)	Fluorescence (EtOH)				Fluorescence (solid)			
No.	position 4	position 6	nm (EtOH)	Ex max(nm)	Em max(nm)	SS[a]	ϕ	Ex max(nm)	Em max(nm)	SS[a]	R.I.[b]
8a	pyrrolidino	C_6H_5	310 (4.08)				0.00	394	448	54	0.44
8b	pyrrolidino	C_6H_4-OMe(4)	311 (4.16)				0.00	391	440	49	0.20
8c	pyrrolidino	C_6H_3-$(OMe)_2$(3,4)	310 (4.17)				0.00	357	444	87	1.42
8d	pyrrolidino	C_6H_3-$(OMe)_2$(2,5)	315 (4.14)				0.00	348	440	92	0.01
8e	pyrrolidino	C_6H_2-$(OMe)_3$(3,4,5)	343 (3.84)				0.00	345	459	104	5.93

[a] Stoke's Shift = Em max(nm) - Ex max(nm).

[b] Relative intensity of fluorescence in solid state, using Alq_3 as a standard.

[c] insufficient solubility.

Table 4.

Computed UV-vis λ max (nm) and oscillator strengths of 3, 5, 6.

	B3LYP	PBE0
3a	339/0.48	332/0.50
3b	355/0.73	347/0.74
3c	358/0.69	348/0.72
3d	398/0.10	379/0.13
3e	351/0.50	341/0.56
3f	412/0.87	400/0.92
3g	363/0.96	352/0.98
3h	360/0.95	351/0.96
3i	361/0.60	353/0.61
3j	368/0.67	360/0.69
3k	397/1.10	387/1.13
3l	480/1.40	467/1.46
5a	319/0.31	310/0.34
5b	325/0.64	317/0.66
5c	335/0.61	325/0.65
5d	352/0.21	340/0.25
5e	346/0.52	337/0.58
6a	317/0.34	308/0.41
6b	339/0.82	329/0.86
6c	324/0.61	315/0.66
6d	383/0.07	365/0.08
6e	316/0.39	307/0.50
6f	373/0.77	361/0.82
6g	330/0.73	320/0.79
6h	329/0.05	317/0.07
6j	320/0.51	312/0.58
6l	404/1.19	392/1.25

Table 5.

Computed UV-vis first intense λ max (nm) of 7a and 8a.

	7a							8a						
	Expl-geom[a]				Optgeom[b]			Expl-geom[a]				Optgeom[b]		
	Vac-monomer	Vac-dimer-1	Vac-dimer-2	ONIOM	Vac-monomer	LS-PCM-monomer	SS-PCM-monomer	Vac-monomer	Vac-dimer1	Vac-dimer1	ONIOM	Vac-monomer	LS-PCM-monomer	SS-PCM-monomer
TD(B3LYP)/6-31G(d)	331	340	371	331	337	329	337	331	340	345	331	331	309	314
TD(B3LYP)/6-31G(d,p)	331	341	371	331	337	329	337	332	341	345	331	332	309	314
TD(B3LYP)/6-31 + G(d,p)	333	342	370	333	339	329	338	332	341	343	332	333	308	314
TD(PBE0)/6-31G(d)	323	327	345	323	329	322	330	320	325	321	320	320	301	306
TD(PBE0)/6-31 + G(d,p)	325	328	345	325	331	322	331	321	327	320	321	322	300	306
TD(CAM-B3LYP)/6-31G(d)	305	308	308	305	311	308	316	293	295	289	293	295	282	287
TD(CAM-B3LYP)/6-31 + G(d,p)	307	309	309	307	312	308	317	293	296	290	294	295	282	287

a Geometries extracted from crystallorganic data.

b Optimized geometries with DFT(B3LYP)/6-311G(2d,2p).

Table 6.

Computed UV-vis and emission λ max (nm) and oscillator strengths of 7a and 8a using CASSCF and MS-CASPT2.

	7a		8a	
	UV-vis[a]	Fluorescence[b]	UV-vis[a]	Fluorescence[b]
Vac-CAS[c]	302	361	274	332
LR-PCM-CAS	251	344	255	304
Vac-PT2[d]	332/0.21	418/0.31	311/0.14	397/0.37
LR-PCM-PT2	294/0.27	390/0.45	296/0.15	365/0.29

a Geometries optimized DFT(B3LYP)/6-3111G(2d,2p).

b Geometries optimized TDDFT(B3LYP)/6-31 + G(d).

c 4-state-averaged CASSCF(10,10)/ANO-L.

d 4-state-averaged MS-CASPT2(10,10)/ANO-L.

Table 7.

Key geometrical parameters of 7a and 8a in S_0 and S_1 state.

		Interatomic distances			Twist angle	
		r(C4–C7)	r(O1–C12)	r(S1–C9)	ϕ(N1–C7–C4–C2)	
7a						
S_0	X-ray-geom	1.49	1.23	1.74	57.2	
	DFT-geom[a]	1.49	1.23	1.76	58.7	
S_1	TD-geom[b]	1.44	1.25	1.76	32.5	
	ONIOM-geom[c]	1.45	1.27	1.75	45.7	
		Interatomic distances			Twist angle	
		r(C4–C7)	r(O1–C12)	r(S1–C9)	ϕ(C8–C7–C4–C2)	ϕ(C8–C9–N3–C13)
8a						
S_0	X-ray-geom	1.48	1.35	1.24	56.3	1.22
	DFT-geom[a]	1.49	1.35	1.23	62.2	4.52
S_1	TD-geom[b]	1.44	1.39	1.25	24.8	2.32
	ONIOM-geom[c]	1.44	1.35	1.26	39.4	4.57

a Optimized geometries with DFT(B3LYP)/6-311G(2d,2p).

b Optimized geometries with TDDFT(B3LYP)/6-31 + G(d).

c Optimized geometries with ONIOM(TD(B3LYP)/6-31 + G(d):PM3).

Table 8.

FMO-TDDFT λ max of 7a and 8a in S_0 and S_1 state.

7a				8a			
UV-vis		Fluorescence		UV-vis		Fluorescence	
FMO-1	FMO-2	FMO-1	FMO-2	FMO-1	FMO-2	FMO-1	FMO-2
320	326	403	415	308	314	392	397

Table 9.

Computed fluorescence λ max (nm) of 3f.

TD-genom[a]

	In vacuo	LR-PCM	SS-PCM
B3LYP	436	437	470
PBE0	424	428	459
CAM-B3LYP	406	398	434

CAS-genom[b]

CAS		PT2	
vac	LR-PCM	vac	LR-PCM
391	346	411	359

a An optimized geometry with TDDFT(B3LYP)/6-31 + G(d).

b An optimized geometry with CASSCF(10e,10o)/ANO-L

Table 10.

Computed fluorescence λ max (nm) and oscillator strengths of 7a and 8a.

	7a		8a	
	TD-geom[a]	ONIOM-geom[b]	TD-geom[a]	ONIOM-geom[b]
TD(B3LYP)/6-31G(d)	446/0.20	421/0.18	463/0.15	435/0.14
TD(B3LYP)/6-31 + G(d,p)	448/0.22	435/0.20	466/0.16	436/0.15
TD(PBE0)/6-31G(d)	432/0.23	421/0.22	445/0.17	418/0.16
TD(PBE0)/6-31 + G(d,p)	434/0.25	421/0.22	447/0.18	419/0.17
TD(CAM-B3LYP)/6-31G(d)	398/0.31	387/0.27	395/0.26	371/0.24
TD(CAM-B3LYP)/6-31 + G(d,p)	400/0.33	387/0.29	397/0.27	371/0.25

a TD(B3LYP)/6-31 + G(d).

b ONIOM(TD(B3LYP)/6-31 + G(d):PM3).